Tunable factors and domain mechanisms for the negative dielectric permittivity of nanofilms in ultrafast time scale

Ming-Ran Zhang(张明冉)[1,2], Rui Ma(马瑞)[1,2,†], Yuan-Xiang Zhang(张元祥)[1,2], and Jian-Qiang Zhou(周建强)[1,2]

[1] *College of Mechanical Engineering, Quzhou University, Quzhou* 324000, *China*

[2] *Zhejiang Key Laboratory of Intelligent Manufacturing for Aerodynamic Equipment, Quzhou* 324000, *China*

(Received 12 January 2026; revised manuscript received 13 April 2026; accepted manuscript online 20 May 2026)

The negative dielectric permittivity of nanofilms holds significant potential for the development of advanced devices. However, the regulatory mechanisms and microscopic origins of this phenomenon on ultrafast time scales remain inadequately understood. Therefore, we investigated the factors governing negative dielectric permittivity in ferroelectric nanofilms on ultrafast time scales and revealed the underlying microscopic mechanisms. A dynamic phase-field model was employed to simulate a $BaTiO_3$ nanofilm with a core-shell grain structure and analyze the effects of the damping coefficient, kinetic coefficient, and electric field amplitude. The results indicated that deviations of the damping coefficient from its optimal value weaken negative dielectric permittivity — lower values enhance positive permittivity, while higher values suppress domain evolution. The kinetic coefficient significantly affects the dielectric permittivity in the high-frequency range, and excessively large or small values tend to inhibit negative dielectric behavior. Larger electric field amplitudes shift the frequency range of negative permittivity toward higher frequencies. These results clarify the microscopic mechanisms underlying the relationship between parameter tuning and negative dielectric permittivity and provide critical insights into optimizing negative dielectric performance in ultrafast ferroelectric-based devices.

Keywords: polycrystalline nanofilm, dynamic phase-field model, negative dielectric permittivity, kinetic coefficient

PACS: 77.80.Dj, 77.22.Ch, 87.15.ht, 77.84.–s

DOI: 10.1088/1674-1056/ae7055 **CSTR:** 32038.14.CPB.ae7055

1. Introduction

Applications of ferroelectric nanofilms span a broad range of areas, including, but not limited to — ferroelectric non-volatile memory, high-density capacitors, high-efficiency energy storage devices, night vision technology, medical ultrasound, actuators, and energy harvesting.[1–4] These applications rely on their distinctive intrinsic properties, such as dielectric response, piezoelectric coefficient, coercive field, and electromechanical and hysteresis loop characteristics[5–7] — properties that can be effectively modulated by tailoring grain structures and microstructural features.[8,9] In practical scenarios, charge defects and domain size in antiferroelectric materials significantly impact polarization switching,[10] and their dynamic response directly dictates device performance.[11,12] Notably, polarization reorientation in ferroelectrics under such loads is an inherently frequency-dependent kinetic process, which in turn induces frequency-dependent electromechanical behaviors. However, research on the dynamic response mechanisms of ferroelectric thin films on ultrafast time scales — particularly regarding the emergence and regulation of negative dielectric permittivity — remains scarce. Existing studies have yet to fully elucidate how fundamental parameters jointly modulate negative dielectric permittivity and its underlying microscopic mechanisms.

Recently, negative dielectric permittivity has attracted substantial attention for its transformative potential in next-generation devices, such as novel steady-state negative capacitors (NC),[13–15] electromagnetic stealth technology,[16] ferroelectric tunnel junctions,[17] and field-effect transistors.[18,19] Initially observed in artificial metamaterials with periodic subwavelength structures,[20,21] negative dielectric permittivity was later identified as an inherent trait of ferroelectric thin films[22,23] and heterostructures,[24] triggered by dielectric resonance within specific frequency ranges.[25,26] Unlike artificial metamaterials, the negative dielectric permittivity of ferroelectric nanofilms can be regulated by leveraging intrinsic properties through adjustments to composition and microstructure. For instance, Yang *et al.*[27] and Thanh *et al.*[28] reported dielectric resonance and negative dielectric permittivity in high-frequency ranges by accounting for polarization dynamics, mimicking the behavior of left-handed materials. Fan, Wang, and colleagues[29–32] explored radio-frequency negative dielectric behavior and dielectric resonance in barium titanate-based composites, demonstrating that the frequency range of negative dielectric behavior can be tuned via physical parameters, composition, and phase structure. At the atomic and theoretical levels, Zhilyaev *et al.*[33] investigated ultrafast polarization switching in barium titanate using density functional theory (DFT) and coupled oscillator models, while Prosandeev *et al.*[34] uncovered negative dielectric permittivity at ultrashort

†Corresponding author. E-mail: marui_sy@163.com

© 2026 Chinese Physical Society and IOP Publishing Ltd. All rights, including for text and data mining, AI training, and similar technologies, are reserved.

CPB Online In-Press

timescales through atomic simulations, linking it to dynamic polarization oscillations.

Different fields demand different dielectric constants in materials. Dielectric capacitors require high dielectric constants, while wave transmission requires low ones. Thus, tuning dielectric constants is a key research area in electromagnetic materials. Traditionally, these constants are positive, but the advent of negative dielectric materials has expanded the possibilities for regulation and introduced new properties and applications. The following discussion focuses on methods for regulating the dielectric properties of materials with intrinsic negative dielectric behavior. Qi *et al.*[35] demonstrated that when the nitrogen-doped carbon content reaches 20 wt%, the composite material exhibits negative dielectric behavior characterized by low-frequency scattering within the frequency range of 10 kHz to 1 MHz, with the negative dielectric constant stabilizing around −40. This phenomenon is attributed to strategies aimed at reducing the plasma frequency of the composite material, consequently enhancing the magnitude of the negative dielectric constant. Wang *et al.*[36] found that increasing direct-current (DC) bias voltage enhances the negative dielectric properties of carbon fiber/quartz ceramic composites. Higher free electron concentrations lead to a larger absolute value and a broader frequency range of the negative dielectric constant. Some composite materials lack components with spontaneous dipoles and dielectric resonances, yet their structures can induce strong dielectric resonances, influencing the dispersion characteristics of negative dielectrics.[37] Haldar *et al.*[38] prepared carbon nanotube/glass composite materials and found that the negative dielectric constant and its frequency range can be precisely controlled by changing the carbon nanotube content. In short, the negative dielectric properties can be regulated by controlling external conditions, as external fields can change the types, quantities, and motion states of charge carriers within the material, thereby affecting its negative dielectric properties.

In addition, NC is a key mechanism for overcoming the Boltzmann tyranny in low-power electronics. Recent studies have established a three-dimensional (3D) Gibbs free-energy landscape for ferroelectric/dielectric heterostructures, clarifying that depolarization effects stabilize quasi-static NC and that single-domain switching becomes dominant at low dielectric capacitance.[39] Traditional perovskite ferroelectrics like lead zirconate titanate (PZT) and $BaTiO_3$ can achieve negative-slope polarization in $P-E$ loops through defect dipole engineering. In acceptor-doped $BaTiO_3$, defect dipoles perpendicular to the external field create a restoring force, leading to intrinsic negative capacitance within specific defect concentrations and temperature ranges.[40] The $BaTiO_3$/TiN composite system offers adjustable negative dielectric constants in the radio-frequency range. Below the percolation threshold, it exhibits Maxwell-Wagner interfacial polarization, while above it, negative dielectric behavior arises from Ti^{4+} ion dielectric resonance and conductive network inductance, with the annealing temperature significantly affecting this behavior.[41] Chen *et al.*[42] achieved ultralow subthreshold swings below 60 mV/dec by pairing ferroelectric and dielectric capacitors. They proposed that the thickness of the ferroelectric layer, residual polarization, coercive field, and interface defects are key parameters for regulating device performance.

Although the aforementioned studies have yielded promising results, the underlying theories remain incomplete, particularly concerning the regulatory mechanisms governing fundamental dielectric resonance characteristics — such as amplitude, damping, and bandwidth — and the conditions under which negative dielectric properties emerge. These issues warrant further investigation. The phase-field method offers crucial theoretical insights into ferroelectric materials and has been used to investigate a broad range of phase-transformation issues.[43–46] In this work, we constructed a core-shell model of polycrystalline $BaTiO_3$ nanofilms and explored the influence of the damping coefficient, kinetic coefficient, and electric field amplitude on negative dielectric behavior using the dynamic phase-field method. The hysteresis and butterfly loops of the nanofilms under different parameter conditions were numerically obtained. The underlying mechanisms were discussed based on the evolution of domain structures in the phase-field simulation results.

2. Theory and model

2.1. The dynamical ferroelectric phase-field method

In the dynamic phase-field simulation, the three components of the electrical polarization vector $\boldsymbol{P}$ serve as the order parameters. The constitutive equations for the mechanical and electrical aspects are

$$\begin{cases} \sigma_{ij} = c_{ijkl}\left(\varepsilon_{kl} - \varepsilon^{*}_{kl}\right), \\ D_i = \kappa_0 E_i + P_i, \end{cases} \tag{1}$$

where c_{ijkl} are the components of the elastic moduli, κ_0 is the permittivity of free space, and ε^{*}_{kl} is the spontaneous strain. Under the assumption of linear kinematics, the strain components ε_{ij} are calculated by $\varepsilon_{ij} = (u_{i,j} + u_{j,i})/2$. In addition, the Helmholtz free energy density (including the free space occupied by the material) is expressed as $\psi = \psi(\varepsilon_{ij}, D_i, P_i, P_{i,j})$. The total free energy F is given by the volume integral of the free energy density ψ, as

$$F = \iiint \psi(\varepsilon_{ij}, D_i, P_i, P_{i,j})\,\mathrm{d}V, \tag{2}$$

where P_i is the polarization vector, $P_{i,j}\left(P_{i,j} = \partial P_i/\partial x_j\right)$ is its gradient, D_i is the electric displacement vector, and ε_{ij} is the strain tensor. The Landau–Ginzburg–Devonshire energy density function for $BaTiO_3$ during its transition from the cubic to the tetragonal phase is generally expressed as[47]

CPB Online First Press

$$\psi(P_i,P_{i,j},\varepsilon_{ij},D_i) = \frac{1}{2}a_{ijkl}P_{i,j}P_{k,l} + \left\{\frac{1}{2}\bar{a}_{ij}P_iP_j + \frac{1}{2}\bar{\bar{a}}_{ijkl}P_iP_jP_kP_l + \frac{1}{6}\bar{\bar{\bar{a}}}_{ijklmn}P_iP_jP_kP_lP_mP_n + \frac{1}{8}\bar{\bar{\bar{\bar{a}}}}_{ijklmnrs}P_iP_jP_kP_lP_mP_nP_rP_s\right\}$$
$$+\left\{b_{ijkl}\varepsilon_{ij}P_kP_l + \frac{1}{2}c^H_{ijkl}\varepsilon_{ij}\varepsilon_{kl} + f_{ijklmn}\varepsilon_{ij}\varepsilon_{kl}P_mP_n + g_{ijklmn}\varepsilon_{ij}P_kP_lP_mP_n\right\} + \frac{1}{2\kappa_0}(D_i-P_i)(D_i-P_i), \quad (3)$$

where the first term denotes the gradient energy associated with diffuse domain walls, commonly called the exchange energy. Within the first brace, the four terms represent the Landau-type energy, which is used to construct the non-convex free-energy landscape with minima at the spontaneous polarization states. The second set of four terms models the spontaneous strain and the dielectric, elastic, and piezoelectric characteristics associated with the spontaneous state. The final term represents the energy stored in the free space, and κ_0 is the permittivity of free space.

It is important to recognize that the conventional TDGL kinetic equation may not be suitable for dynamics under ultrafast stimuli lasting less than 100 ns.[48] We therefore developed a dynamic phase-field model incorporating a second-order time derivative of polarization to analyze the electrical behavior and microstructural dynamics of ferroelectric nanomaterials under dynamic conditions.[49] The second-order polarization dynamics equation takes the generalized form

$$\left(\frac{\partial\psi}{\partial P_{i,j}}\right)_{,j} - \frac{\partial\psi}{\partial P_i} + \gamma_i = \beta_{ij}\dot{P}_j + \mu_{ij}\ddot{P}_j, \quad \text{in} \quad V. \quad (4)$$

Here, the kinetic coefficients μ_{ij}, which represent the effective mass density of the material, and β_{ij}, which represent the damping coefficients of the system, are related to domain-wall mobility. They link the frequency of the applied electric field to the dynamic microstructural response of ferroelectric crystals and describe the relationship between the rate of change of polarization over time and the thermodynamic driving force. Direct experimental measurement of these values is challenging; however, they can be obtained indirectly by comparing phase-field simulations with relevant experimental observations.[50] $\bar{\beta}$, also known as the inverse "mobility" tensor, can be expressed as $\bar{\beta} = 1/L = 0.25\times10^6\ \mathrm{m^2\cdot N\cdot s\cdot C^{-2}}$, according to Ref. [47]. Here, the mobility tensor is $L = 4\times10^{-6}\ \mathrm{C^2\cdot m^{-2}\cdot N^{-1}\cdot s^{-1}}$, which has been successfully applied in other phase-field simulations.[6,51,52] The supplemental files from Akamatsu *et al.*[50] indicate that the damping frequency in the oscillation model is given by $\gamma = \bar{\beta}/\mu \approx 0.03$–$5\ \mathrm{ns^{-1}}$, where the effective mass density for the dynamic phase-field method is chosen as $\mu = 0.7\times10^{-2}\ \mathrm{m^2\cdot N\cdot s^2\cdot C^{-2}}$. Picinin *et al.*[53] also postulated a constant kinetic coefficient in the dynamic control equation, yielding experimental results that closely agree with simulations. Consequently, this assumption is adequate for most non-diffusive phase transitions. On ultrafast time scales, Eq. (4) describes the frequency dependence of distinctive dynamic properties, including the dielectric coefficient at zero electric field, remanent polarization, and coercive field.

It should be noted that Eq. (4) differs from the equations adopted in existing DFT and coupled-oscillator models.[33] DFT is a foundational theoretical framework widely employed in first-principles calculations and grounded in quantum mechanics to investigate microscopic properties such as electronic states, bonding, and defect energies. The dynamic phase-field theory used in this study operates at the mesoscale and is designed to simulate microstructural evolution during nonequilibrium processes. The novelty of this research lies in applying a nonequilibrium continuum thermodynamic framework to derive the polarization dynamics equation. The continuum-based strategy used to derive the evolution equation is thermodynamically sound and provides a natural basis for the finite element technique used to determine unknown electromechanical fields simultaneously. Additionally, Eq. (4) reveals distinctive dynamic features at ultrafast time scales, such as the dielectric constant and coercive field, which can be observed through hysteresis loops. It also allows polarization states to be tracked over time to characterize macroscopic dynamics and explore the microscopic mechanisms of negative dielectric behavior within specific frequency ranges.

By combining the equation of motion ($\sigma_{ji,j} + b_i = \rho\ddot{u}_i$ in V), Maxwell's electrical equations, the Maxwell equation ($D_{i,i} - q = 0$ in V), and the dynamic equation (Eq. (4)) governing the evolution of electric domains, and then organizing and deriving the resulting equations, the following virtual work equation can be obtained:

$$\begin{aligned}&\int_V \beta_{ij}\dot{P}_j\delta P_i\mathrm{d}V + \int_V \mu_{ij}\ddot{P}_j\delta P_i\mathrm{d}V + \int_V \rho\ddot{u}_i\delta u_i\mathrm{d}V\\ &+\int_V(\sigma_{ji}\delta\varepsilon_{ij} - D_i\delta E_i + \eta_i\delta P_i + \xi_{ji}\delta P_{i,j})\mathrm{d}V\\ =&\int_V(b_i\delta u_i - q\delta\phi + \gamma_i\delta P_i)\mathrm{d}V\\ &+\int_S(t_i\delta u_i - \omega\delta\phi + \xi_{ji}n_j\delta P_i)\mathrm{d}S. \end{aligned} \quad (5)$$

The virtual work Eq. (5) provides the basis for finite element discretization of the phase-field model. Combined with the constitutive relations of ferroelectric materials, it can be used to formulate the corresponding finite element programs. The finite element approach allows unknowns such as displacement, electric potential, and electrical polarization to be determined simultaneously. For more comprehensive information

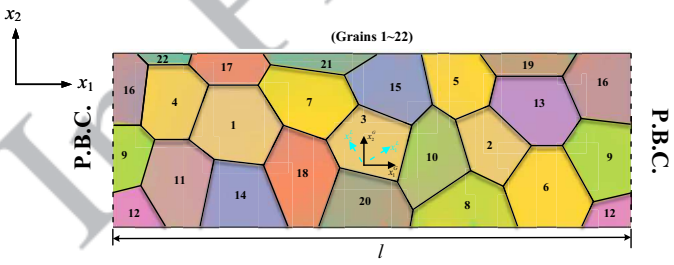
CPB Online In Press

on numerical approaches to phase-field methods, readers are referred to Refs. [6,47,54].

2.1.1. The nano-grained $BaTiO_3$ thin film model

Polycrystalline thin films exhibit highly complex grain structures with inherent structural characteristics and are composed of grains with varying lattice orientations. The interfaces between adjacent grains possess properties distinct from those within the grains themselves. The nanograins are presumed to have a core-shell structure resulting from the uneven diffusion and phase segregation of dopants and defects during the crystallization and annealing of $BaTiO_3$ nanofilms.[54,55] At low temperatures or under rapid heating, defects such as dopant ions and oxygen vacancies concentrate at grain surfaces and boundaries, creating a distinct core-shell configuration in which a low-polarization, low-dielectric shell surrounds a highly polarized ferroelectric grain. The formation of this structure is primarily governed by the thermodynamic driving force to reduce interfacial energy and alleviate grain-boundary stress. Additionally, it is influenced by the dynamics of constrained atomic diffusion at medium and low temperatures. Consequently, dopants are not fully homogenized, thereby maintaining pronounced compositional and property gradients between the core and shell regions.

The core-shell model, as depicted in Fig. 1, features a grain boundary (black solid line) and the interiors of nanograins (multicolored regions). The grain boundary (GB) is treated as a "dead layer" with no polarization and a dielectric permittivity equal to 35% of that of the grain interior. During the fabrication of polycrystalline thin films, material defects frequently arise, leading to differences in the mechanical and electrical properties between grain boundaries and grain interiors. Patrick Fedeli *et al.*[56] substantiated these differences in material properties through both experimental observations and phase-field simulations. In this study, the dielectric constant of the grain boundary was set to 250, a value calibrated against existing literature to achieve agreement with experimental results while remaining within a plausible range. Previous studies[57–59] have shown that the dielectric constant of grain boundaries should be investigated comprehensively through experimental measurements, such as impedance spectroscopy and scanning probe microscopy, and theoretical simulations. These studies combined experimental analyses with effective-medium modeling to infer the ratio of the grain-boundary dielectric constant to the grain-interior dielectric constant, obtaining a range of 0.2–0.4, which agrees well with the experimentally observed relationship between dielectric constant and grain size. Hence, a value of 0.35 was chosen as a representative and physically reasonable parameter within this well-documented interval. In addition, this assumption is widely adopted in the literature on $BaTiO_3$ polycrystals and thin films, as grain boundaries are non-ferroelectric "dead layers" with significantly suppressed polarization.[6,51,52,60] The thickness of the grain boundary is 2–3 atomic spacings (0.8 nm) and remains constant regardless of grain size.[61] Smaller grains enhance the manifestation of complex domain structures and electromechanical behaviors in ferroelectric polycrystalline materials,[62] so the average grain size was set to 15 nm. We assumed a two-dimensional planar model for the nanofilm, with equal in-plane strains in the x_1 and x_3 directions under a biaxial strain condition. As illustrated in Fig. 1, the two-dimensional unit comprises 22 nanograins with different local crystal lattice orientations, characterized by the rotation angle φ between the global coordinates x_i^G and the local coordinates x_i^L $(i=1,2)$, ranging from 0° to 90°.



(Angles 0°~90°)

①	②	③	④	⑤	⑥	⑦	⑧	⑨	⑩	⑪
0°	4.09°	8.18°	12.27°	16.36°	20.45°	24.54°	28.63°	32.72°	36.81°	40.9°
⑫	⑬	⑭	⑮	⑯	⑰	⑱	⑲	⑳	㉑	㉒
45°	49.09°	53.18°	57.27°	61.36°	64.45°	69.54°	73.63°	77.72°	81.18°	85.9°

Fig. 1. Representative unit of the $BaTiO_3$ polycrystalline nanofilm comprising twenty-two nanograins.

All computations are carried out assuming a planar model, with the x_3-components of physical quantities being zero, i.e., $P_3=0$, $E_3=0$, $D_3=0$, $\sigma_{13}=\sigma_{23}=0$. Assuming a 2D planar model, we define the constant strain component as the mismatch strain ($\varepsilon_{11}=\varepsilon_{33}=\bar{\varepsilon}$), which must be included in all subsequent calculations involving a constitutive relation. The mismatch strain is set to -0.1%.[63] Periodic mechanical and electrical boundary conditions are applied to the film's sides ($u_1|_{x_1=0}=u_1|_{x_1=l}+l\bar{\varepsilon}$, $u_2|_{x_1=0}=u_2|_{x_1=l}$, $\phi|_{x_1=0}=\phi|_{x_1=l}$ and $P_i|_{x_1=0}=P_i|_{x_1=l}$ $(i=1,2)$), with in-plane strain introduced via displacement conditions. The bottom displacement's x_2-component is constrained to simulate substrate effects, and the electric potential there is set to zero. The top surface is stress-free, with its electric potential adjusted to generate a time-dependent sinusoidal electric field through the film, given by $hE_{\max}\sin(2\pi f\cdot t)$. Here, $E_{\max}$ is the amplitude of the AC field, h is the thickness of the nanofilm, and t is the real time. We set $E_{\max}=8E_0$, where E_0 represents the electric field required to fully switch a uniform domain in a $BaTiO_3$ crystal and is equal to 218 kV/cm.[6,47,51] The material constants used in this phase-field simulation are taken from Su and Landis.[47]

CPB Online Ip Press

3. Results and discussion

3.1. Tuning the damping coefficient β

The calculated hysteresis loops and butterfly loops at the selected damping coefficients ($0.05\bar{\beta}$, $0.1\bar{\beta}$, $0.3\bar{\beta}$, $0.5\bar{\beta}$, $\bar{\beta}$ and $2\bar{\beta}$) and a frequency of 40 kHz are plotted in Figs. 2(a) and 2(b). A damping coefficient of $0.5\bar{\beta}$ results in the maximum negative dielectric permittivity at zero electric field, as illustrated in Fig. 2(a). Damping coefficients that deviate significantly from this value, either larger or smaller, are less favorable for generating negative dielectric permittivity.

Specifically, when the damping coefficient is below $0.3\bar{\beta}$, its effect on domain wall motion in the ultrafast dynamic equation is negligible, leading to increased positive dielectric permittivity. Conversely, when the damping coefficient exceeds $0.5\bar{\beta}$, the negative dielectric permittivity diminishes progressively, as an excessively large damping coefficient can inhibit the evolution of domain structures. Furthermore, as depicted in the butterfly loops in Fig. 2(b), an increase in the damping coefficient reduces both the piezoelectric coefficient and the actuation strain (the difference between the maximum and minimum strains) of the ferroelectric thin film, thereby impeding the rate of polarization reversal. Once the damping coefficient exceeds $0.5\bar{\beta}$, the 'tails' of the butterfly loops become invisible, confirming the suppression of polarization switching in the nanofilms. The dielectric permittivity at zero electric field and the remnant polarization were calculated from the hysteresis loops in Fig. 2(a). The trends in these values for the selected damping coefficients are summarized in Fig. 2(c). The dielectric permittivity decreases drastically as the damping coefficient increases to $0.5\bar{\beta}$, and then rises as the damping coefficient increases to $2\bar{\beta}$. The remnant polarization exhibits a rise-then-drop trend as the damping coefficient increases.

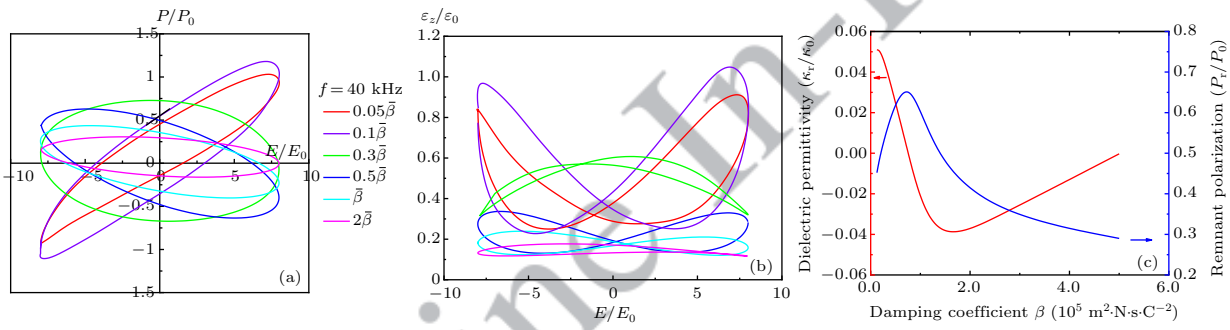


Fig. 2. Computed effects of the damping coefficient on (a) the hysteresis loops and (b) the butterfly loops of the $BaTiO_3$ polycrystalline nanofilm at 40 kHz; (c) variations in the remnant polarization and the dielectric permittivity at zero electric field with the damping coefficient.

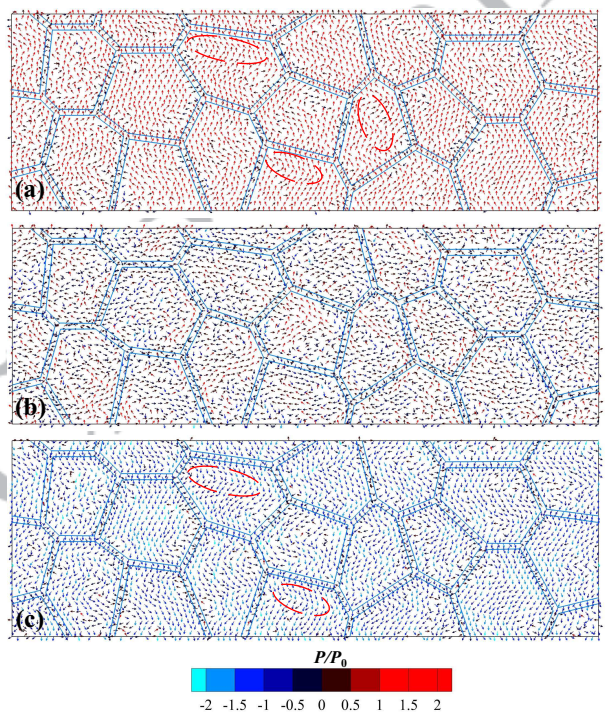


Fig. 3. Polarization distributions in the $BaTiO_3$ polycrystalline nanofilm with a damping coefficient of $0.1\bar{\beta}$: (a) maximum positive electric field ($E = 8E_0$); (b) remnant polarization state ($E = 0$); and (c) maximum negative electric field ($E = -8E_0$).

Importantly, the "optimal damping value $0.5\bar{\beta}$" discussed in this article refers to the damping value that maximizes the negative dielectric constant at a given frequency, thereby achieving an optimal balance between the speed of polarization response and energy dissipation. The damping coefficient quantifies the resistance of ferroelectric materials to oscillations, with its microscopic origins primarily attributed to domain-wall pinning and frictional resistance arising from grain boundaries, phonon scattering, and lattice dissipation. When the damping is below the optimal value (underdamping), the domain structure rapidly switches and exhibits pronounced oscillations, resulting in a phase angle between the polarization and the external electric field of less than 90°. Consequently, the polarization vector has sufficient time to reach saturation, and the hysteresis loop assumes a typical shape, with the dielectric constant remaining positive. Conversely, when the damping exceeds the optimal value (overdamping), domain-wall motion is significantly impeded, preventing the polarization from effectively responding to external fields. Under these conditions, the phase-angle requirements for a negative dielectric response are not satisfied, leading to a substantial weakening or even disappearance of the negative dielectric response.

The impact of the damping coefficient on the negative di-

electric permittivity of thin films is illustrated by the variations in the hysteresis loops, as depicted in Fig. 2(a). To better understand how damping influences the negative dielectric properties of ferroelectric thin films, we examined the microstructural evolution of $BaTiO_3$ polycrystalline thin films under different damping coefficients, as shown in Figs. 3 and 4.

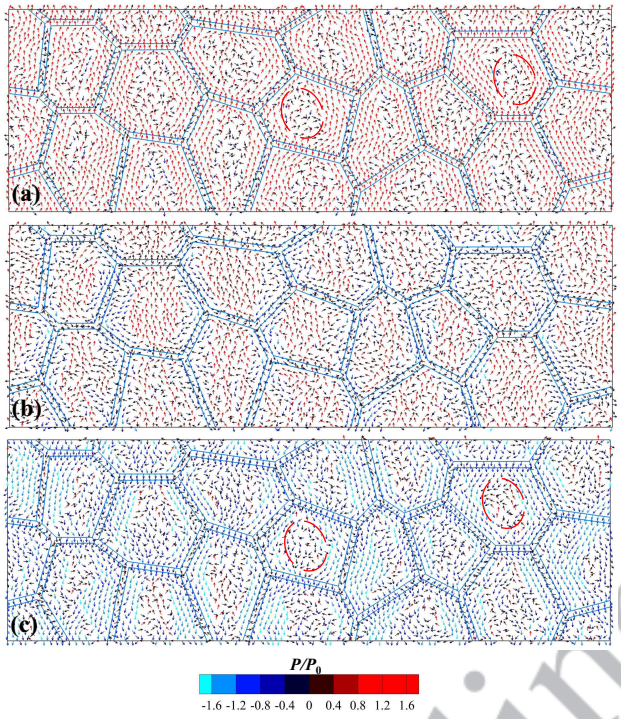


Fig. 4. Polarization distributions in the $BaTiO_3$ polycrystalline nanofilm with a damping coefficient of $0.3\bar{\beta}$: (a) positive remnant polarization state ($E = 0$); (b) maximum negative electric field state ($E = -8E_0$); and (c) negative remnant polarization state ($E = 0$).

This analysis aims to elucidate the microscopic mechanisms underlying the effect of the damping coefficient on the negative dielectric permittivity at zero electric field. Specifically, Figs. 3(a)–3(c) show that, as the damping coefficient changes, the polarization vectors of most grains undergo a 180° flip during cyclic loading and unloading of the electric field. In Figs. 3(a) and 3(c), under maximum positive or negative electric field conditions, some grains exhibit 90° domain structures. In the remnant polarization state ($E = 0$), as shown in Fig. 3(b), the polarization vectors within the film exhibit an overall disordered distribution. Wang *et al.*[31] demonstrated that an increase in the damping coefficient significantly enhances the collective resonance of surface charges, thereby inhibiting polarization reversal. This inhibition impedes the ability of interface polarization to adapt to variations in the applied electric field, ultimately leading to the gradual development of negative dielectric permittivity. As illustrated in Figs. 4(a)–4(c), when the damping coefficient increases to $0.3\bar{\beta}$, the hysteresis loop assumes an elliptical shape, and the coercive field increases sharply. The pronounced oscillation of the electric dipole prevents the polarization vector within the crystal nucleus from completing a 180° rotation during cyclic loading and unloading of the electric field, further confirming the inhibitory effect of the damping coefficient on the rate of polarization reversal. When the damping coefficient reaches $0.5\bar{\beta}$, the polarization vector lags behind the electric field by half a cycle, and the negative dielectric permittivity reaches its maximum magnitude.

3.2. The factor of kinetic coefficients μ_{ij}

In the second section of this article, we discussed the kinetic coefficient μ, which is associated with the second derivative of polarization in the second-order polarization dynamic equation. This coefficient represents the effective mass density of the material and is linked to the mobility of domain walls. Figures 5–7 provide a comprehensive examination of how the kinetic coefficient influences the negative dielectric properties of ferroelectric thin films from two perspectives: hysteresis loops and domain structure evolution. Specifically, Figs. 5(a)–5(c) illustrate the effects of loading frequency on the hysteresis loops of the thin film for three distinct kinetic coefficients (0.1μ, 1μ, and 10μ), while Fig. 5(d) summarizes the corresponding dielectric permittivity as a function of frequency at zero electric field.

The findings suggest that within the low-frequency range (below 10 kHz), variations in the kinetic coefficient have minimal influence on the dielectric permittivity. However, as the frequency increases, the kinetic coefficient increasingly affects the hysteresis loop. Specifically, when the kinetic coefficient is 0.1μ, as depicted in Fig. 5(a), the smaller kinetic coefficient diminishes the influence of polarization oscillations, although negative dielectric permittivity emerges at higher frequencies, consistent with the results obtained using conventional phase-field methods. As illustrated in Fig. 5(b), when the kinetic coefficient increases to μ, dipole vibrations intensify, and the negative dielectric permittivity reaches its maximum magnitude at a frequency of 40 kHz. A further increase in the kinetic coefficient, as shown in Fig. 5(c), shifts the peak magnitude of the negative dielectric permittivity to 20 kHz. However, as depicted in Fig. 5(d), an excessively large kinetic coefficient inhibits polarization reversal, reducing the remnant polarization and thereby weakening the negative dielectric response.

It should be noted that the kinetic coefficient characterizes both the rate of polarization reversal and the velocity of domain-wall motion. The relaxation time associated with domain structure switching is inversely proportional to this coefficient. A larger kinetic coefficient indicates reduced resistance to domain-wall motion, resulting in a more rapid polarization response and a shorter relaxation time. At low external-field frequencies, the polarization closely follows changes in the external field, exhibiting minimal hysteresis, and the dielectric response is typical of a conventional positive dielectric. The frequency-dependent negative dielectric response can be explained as follows. As the frequency increases, polarization reversal induces a phase shift, causing the real part of

CPB Online In-Press

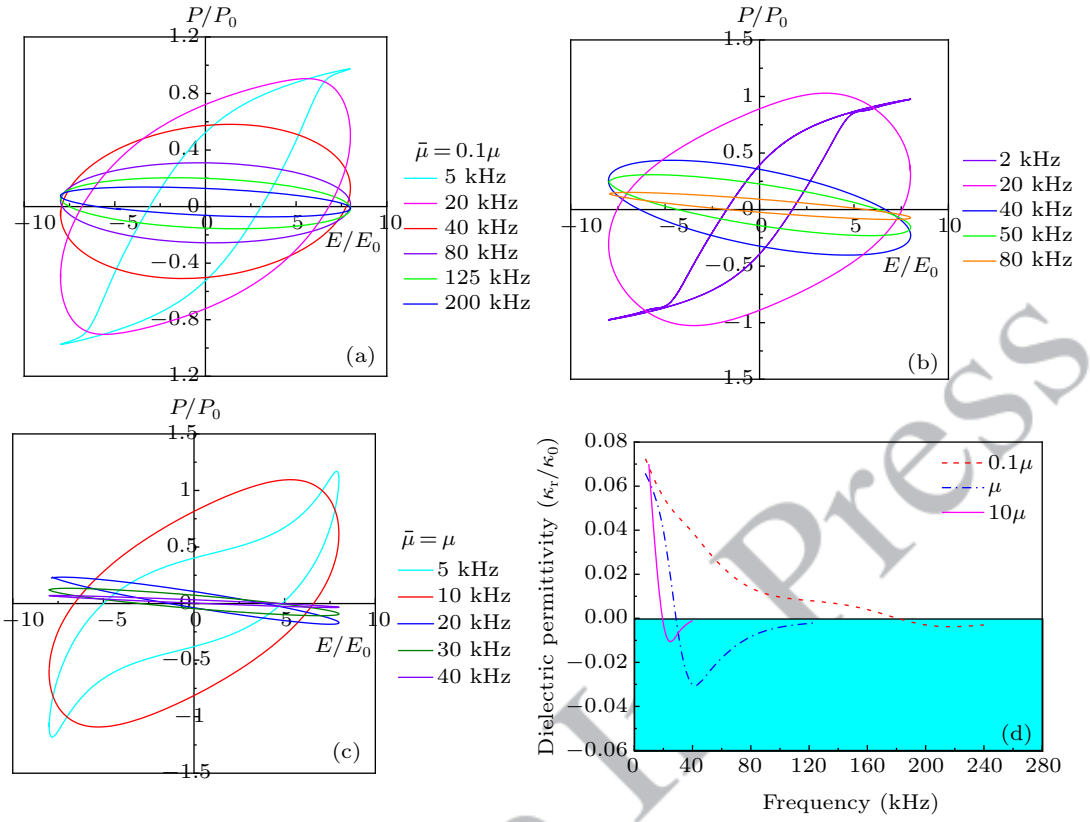


Fig. 5. Effects of loading frequency on the hysteresis loops of $BaTiO_3$ polycrystalline nanofilms with kinetic coefficients of (a) 0.1μ, (b) μ, and (c) 10μ; (d) computed dielectric permittivity at zero electric field as a function of frequency for the three kinetic coefficients.

the dielectric constant to become negative. However, as the external-field frequency continues to rise, the polarization can no longer respond effectively, and the negative dielectric response becomes less pronounced.

The microscopic mechanisms underlying the influence of the kinetic coefficient on negative dielectric permittivity were investigated by analyzing the microstructural evolution in the dynamical phase-field simulations of the nanograins. We plotted the domain structures at 20 kHz for kinetic coefficients of 0.1μ and 10μ, as shown in Figs. 6 and 7, respectively.

When the kinetic coefficient is 0.1μ, as shown in Fig. 5(a), the hysteresis loop has a typical shape and exhibits a larger positive dielectric permittivity. The microstructural evolution shown in Figs. 6(a)–6(c) indicates that the polarization vector within the thin film undergoes a 180° reversal during electric-field loading, unloading, and reverse loading. In Figs. 6(a) and 6(c), the states corresponding to the maximum positive and negative electric fields exhibit single-domain patterns, with the polarization vector oriented vertically upward and downward, respectively. At the coercive-field state, as depicted in Fig. 5(b), the overall polarization was zero. The findings suggest that a smaller kinetic coefficient has little influence on polarization reversal. However, when the kinetic coefficient increases to 10μ, as demonstrated in Figs. 7(a)–7(c), the excessively large kinetic coefficient inhibits domain structure evolution, preventing the polarization vector from completing a 180° reversal. At the maximum positive and negative electric fields, as shown in Figs. 7(a) and 7(c), multiple domain patterns, including 90° and 180° domains, are observed in certain grains. Additionally, at the coercive-field state, as

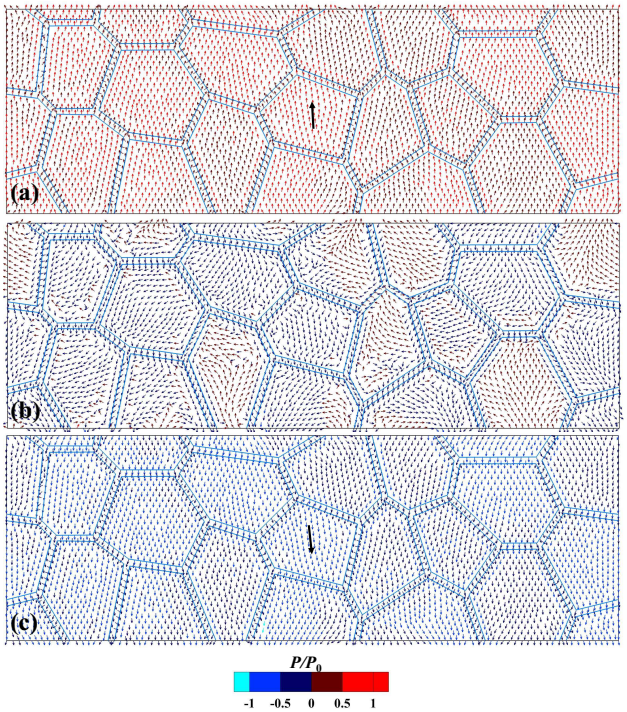


Fig. 6. Polarization distributions in the $BaTiO_3$ polycrystalline nanofilm with a kinetic coefficient of 0.1μ: (a) maximum positive electric field state ($E = 8E_0$); (b) coercive field state ($P = 0$); and (c) maximum negative electric field state ($E = -8E_0$).

CPB Online First Press

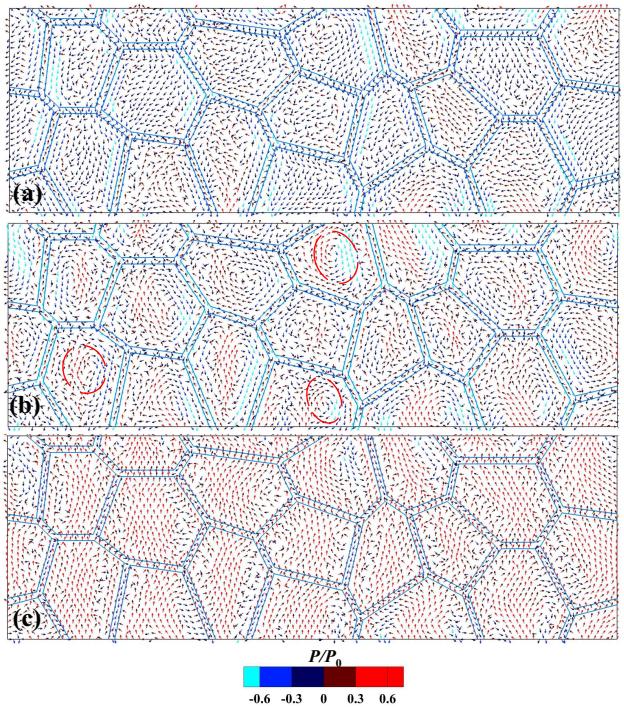


Fig. 7. Polarization distributions in the $BaTiO_3$ polycrystalline nanofilm with a kinetic coefficient of 10μ: (a) maximum positive electric field state ($E = 8E_0$); (b) coercive field state ($P = 0$); and (c) maximum negative electric field state ($E = -8E_0$).

illustrated in Fig. 7(b), numerous vortex-domain structures are present within the film. These structures are unstable and thus contribute to a smaller magnitude of negative dielectric permittivity and a lower coercive field.

3.3. Effect of electric field amplitude E_{max}

Previous research has demonstrated that increased electric field amplitudes in the Ginzburg–Landau equation enhance the thermodynamic driving force and accelerate polarization evolution in polycrystalline barium titanate films. Given that increasing the electric field amplitude accelerates polarization reversal, thereby altering the domain structure within the thin film, it is pertinent to investigate the implications of this negative dielectric behavior within the dynamic phase-field model. Figure 8 illustrates the effect of loading frequency on the hysteresis loops of the thin film under three distinct electric field amplitudes at a tensile strain of 1%. It is evident that higher electric field amplitudes enhance domain-wall mobility, enabling effective competition with high-frequency loading. Three hysteresis loops at different loading frequencies were extracted from Fig. 8 and are summarized in Figs. 9(a)–9(c). Figure 9(d) shows the relationship between the dielectric permittivity and loading frequency for three distinct electric field amplitudes. The analysis reveals that as the electric field amplitude increases, the frequency range over which negative dielectric permittivity occurs in ferroelectric thin films shifts toward higher frequencies. Concurrently, the magnitude of the negative dielectric response decreases. The underlying physical mechanism is directly related to the reduction in the field-induced nucleation barrier, the increase in domain-wall velocity, and the acceleration of nonequilibrium polarization dynamics. The electric field lowers the potential barrier for domain nucleation, accelerating the polarization response and shortening the relaxation time. Consequently, the characteristic frequency at which negative dielectric behavior occurs increases. Enhanced domain-wall velocity allows the system to respond to higher-frequency changes, shifting the negative dielectric window. The strong electric field drives polarization into a high-speed response regime, reducing the time required for polarization changes and thereby causing this shift.

In general, negative dielectric behavior arises from the nonequilibrium response of ferroelectric domain polarization. Under certain frequency and damping conditions, the polarization lags behind the external electric field, leading to a negative dielectric constant. This is a typical nonequilibrium polarization response described by the second-order polarization dynamic phase-field equation. Its microscopic origin is mainly associated with hysteresis and polarization relaxation during domain-wall motion, strong polarization hysteresis caused by grain-boundary interactions, and the depolarization field within the core–shell structure. These factors cause a phase difference between the polarization and the external field, resulting in a negative dielectric constant. This mechanism is analogous to the collective charge resonance in a ferroelectric system under an external alternating electric field proposed by Wang *et al.*[31] It is therefore associated with plasmon-like oscillations of domain walls and the delayed response of bound charges.

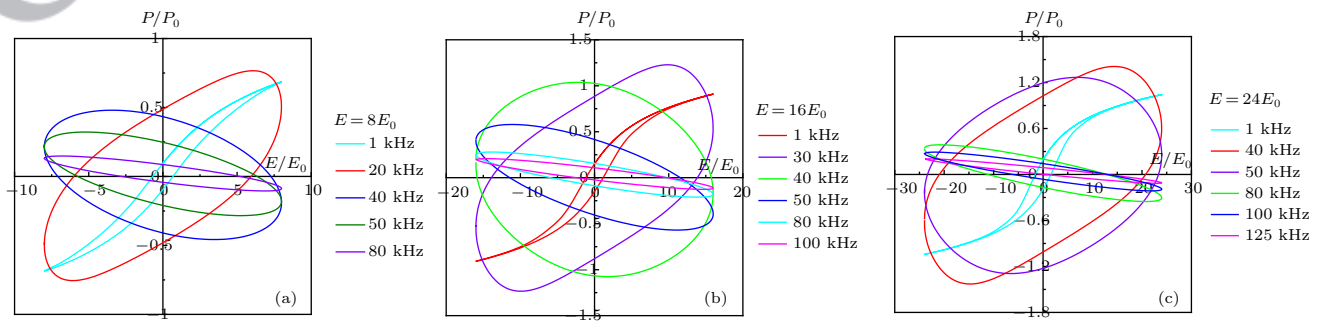


Fig. 8. The calculated effects of different loading frequencies on the hysteresis loops of the nanofilm at electric field amplitudes of (a) $8E_0$, (b) $16E_0$, and (c) $24E_0$.

CPB Online In Press

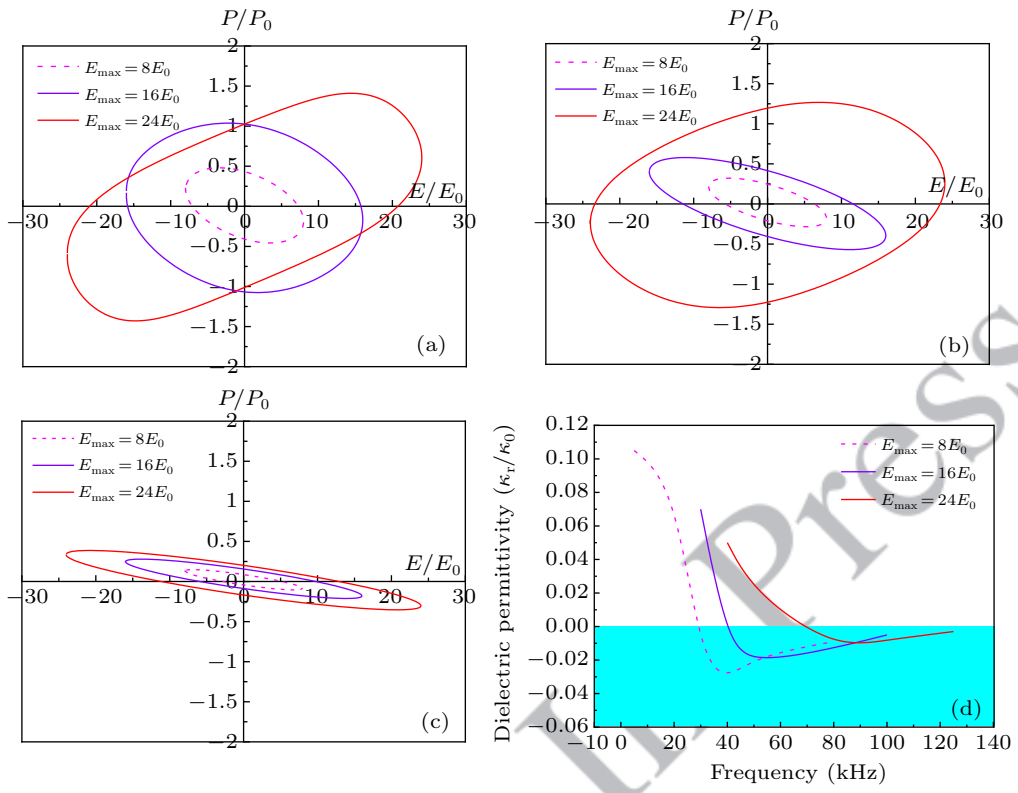


Fig. 9. The calculated effects of electric field amplitude on the hysteresis loops of the nanofilm at loading frequencies of (a) 40 kHz, (b) 50 kHz, and (c) 80 kHz; (d) the calculated dielectric coefficient at zero electric field as a function of frequency for three electric field amplitudes.

4. Conclusion

This study systematically investigates the factors governing negative dielectric permittivity in polycrystalline $BaTiO_3$ ferroelectric nanofilms at ultrafast time scales through dynamic phase-field simulations. The results demonstrate that three parameters — the damping coefficient, kinetic coefficient, and electric field amplitude — exert distinct yet pivotal effects on negative dielectric behavior. Analysis of hysteresis loops and microstructures reveals that a damping coefficient below $0.3\bar{\beta}$ has little effect on polarization reversal, whereas a coefficient above $\bar{\beta}$ suppresses domain switching and weakens the negative dielectric response. Moderate kinetic coefficients induce pronounced dipole vibrations and produce the strongest negative dielectric response, whereas excessively high values trigger the formation of unstable vortex domains, thereby weakening the negative dielectric response. Notably, increasing the electric field amplitude accelerates polarization reversal, shifting the frequency range of negative permittivity toward higher frequencies while reducing the overall magnitude of the negative dielectric response.

Acknowledgments

Project supported by the Zhejiang Provincial Natural Science Foundation of China (Grant Nos. LQN26A020014 and QZQN25E020015), the Quzhou Scientific and Technological Project (Grant No. 2025K197), and the Zhejiang Key Laboratory of Intelligent Manufacturing for Aerodynamic Equipment (Grant No. 2025E10033).

References

[1] Koukhar V G, Pertsev N A and Waser R 2001 *Phys. Rev. B* **64** 214103
[2] Martin L W and Rappe A M 2016 *Nat. Rev. Mater.* **2** 16087
[3] Pan H, Ma J, Ma J, Zhang Q, Liu X, Guan B, Gu L, Zhang X, Zhang Y J, Li L, Shen Y, Lin Y H and Nan C W 2018 *Nat. Commun.* **9** 1813
[4] Das A K, Raul C K, Karmakar R and Meikap A K 2021 *Phys. Lett. A* **407** 127455
[5] Bedoya-Hincapié C M, Ortiz-Álvarez H H, Restrepo-Parra E, Olaya-Flórez J J and Alfonso J E 2015 *Chin. Phys. B* **24** 117701
[6] Zhang Q N, Xia X D, Wang J and Su Y 2018 *Int. J. Solids Struct.* **144–145** 32
[7] Zhang M, Ma R, Zhou J, Zhang Y, Wang J and Weng S 2024 *Coatings* **14** 1437
[8] Ye M, Pan Z, Song W, Liu J, Ye X, Xiong X, Liu H, Fan L, Lu N, Wang R and Long Y 2025 *Chin. Phys. B*
[9] Al-Aaraji M N, Wang B, Feteira A and Hall D A 2025 *Materials* **18** 623
[10] Zhu J, Liu Z, Zhong B, Wang Y and Xu B 2023 *Chin. Phys. B* **32** 047701
[11] Meng X D, Chu L Z, Deng Z C, Zhang P C and Wang Y L 2021 *Ferroelectrics* **571** 200
[12] Tamim H, Khadka R and Keblinski P 2024 *Appl. Phys. Lett.* **125** 102905
[13] Yadav A K, Nelson C T, Hsu S L, Hong Z, Clarkson J D, Schleputz C M, Damodaran A R, Shafer P, Arenholz E, Dedon L R, Chen D, Vishwanath A, Minor A M, Chen L Q, Scott J F, Martin L W and Ramesh R 2016 *Nature* **530** 198
[14] Wang J, Shi Z, Mao F, Chen S and Wang X 2017 *ACS Appl. Mater. Interfaces* **9** 1793
[15] Hou Y F, Li W L, Zhang T D, Yu Y, Han R L and Fei W D 2016 *ACS Appl. Mater. Interfaces* **8** 22354
[16] Schurig D, Mock J J, Justice B J, Cummer S A, Pendry J B, Starr A F and Smith D R 2006 *Science* **314** 977
[17] Li L, Yu J and Zou D 2025 *Phys. Lett. A* **560** 130972

CPB Online First

[18] McGuire F A, Cheng Z H, Price K and Franklin A D 2016 *Appl. Phys. Lett.* **109** 093101
[19] Saeidi A, Rosca T, Memisevic E, Stolichnov I, Cavalieri M, Wernersson L E and Ionescu A M 2020 *Nano Lett.* **20** 3255
[20] Smith D R, Pendry J B and Wiltshire M C 2004 *Science* **305** 788
[21] Liu C, Bai Y, Jing L, Yang Y, Chen H, Zhou J, Zhao Q and Qiao L 2017 *Acta Mater.* **135** 144
[22] Park H W, Roh J, Lee Y B and Hwang C S 2019 *Adv. Mater.* **31** 1805266
[23] Pintilie L, Boni G A, Chirila C, Hrib L, Trupina L, Filip L D and Pintilie I 2020 *Phys. Rev. Appl.* **14** 014080
[24] Hoffmann M, Gui M C, Slesazeck T, Fontanini R, Segatto M, Esseni D and Mikolajick T 2021 *Adv. Funct. Mater.* **32** 2108494
[25] Ciomaga C E, Dumitru I, Mitoseriu L, Galassi C, Iordan A R, Airimioaei M and Palamaru M N 2010 *Scr. Mater.* **62** 610
[26] Guerra J d L S and Eiras J A 2007 *J. Phys.: Condens. Matter* **19** 386217
[27] Bai Y, Zhou J, Sun Y, Li B, Yue Z X, Gui Z L and Li L T 2006 *Appl. Phys. Lett.* **89** 112907
[28] Thanh T D, Dang V N, Hong V L, Phan T L and Yu S C 2014 *J. Korean Phys. Soc.* **65** 1663
[29] Fan G H, Xie P T, Wang Z Y, Qu Y P, Zhang Z D, Liu Y and Fan R H 2017 *Ceram. Int.* **43** 16980
[30] Wang Z Y, Sun K, Xie P T, Liu Y and Fan R H 2017 *J. Phys.: Condens. Matter* **29** 365703
[31] Wang Z Y, Sun K, Xie P T, Hou Q, Liu Y, Gu Q L and Fan R H 2020 *Acta Mater.* **185** 412
[32] Wang Z Y, Fu X Y, Zhang Z D, Jiang Y L, Waqar M, Xie P T, Bi K, Liu Y, Yin X W and Fan R H 2019 *J. Cleaner Prod.* **234** 588
[33] Zhilyaev P, Brekhov K, Mishina E and Tantardini C 2024 *ACS Omega* **9** 4594
[34] Prosandeev S, Paillard C, Xu B and Bellaiche L 2020 *Phys. Rev. B* **101** 024111
[35] Qi Y, Yin R, Wang C, Sun K, Xie P, Song J, Hou Q, Yu Z, Huang Q, Wu H and Fan R 2024 *Adv. Compos. Hybrid Mater.* **8** 18
[36] Wang J, Cheng C, Liu Y, Zhou J, Ma R, Cui H, Hu Z, Zou J, Wang T, Zhao Y and Fan R 2024 *Ceram. Int.* **50** 7538
[37] Du B, Guo Z, Sun Z, Qiu Y, Wang P, Ding H, Tian S and Qian L 2023 *Diamond Relat. Mater.* **139** 110333
[38] Haldar T, Kumar U, Yadav B C and Kumar V V R K 2020 *J. Mater. Sci.: Mater. Electron.* **31** 11791
[39] Li B, Zhang X, Zhu D, Yang H, Wang X, Jiang J, Di Y, Zhang L, Wu J and Yin Z 2025 *J. Appl. Phys.* **137** 224101
[40] Li Z, Qin S, Li J, Su Y, Qiao L, Liu C and Bai Y 2024 *Acta Mater.* **277** 120224
[41] Swetha P, Vidyadharan D M, Sridharan K, T. H M S, M B and Swaminathan S 2024 *Mater. Chem. Phys.* **317** 129156
[42] Chen R S and Lu Y 2024 *Small* **20** 2304445
[43] Li X X and Xu Y 2022 *Int. J. Solids Struct.* **234–235** 111259
[44] Yu X, Li H and Su Y 2025 *Int. J. Solids Struct.* **316** 113392
[45] Huang X, Yang F, Du L, Wang J, Liang Y and Wu P 2025 *Materials* **18** 3606
[46] Shao C and Huang H 2025 *Chin. Phys. B* **34** 027701
[47] Su Y and Landis C M 2007 *J. Mech. Phys. Solids* **55** 280
[48] Yang T, Wang B, Hu J M and Chen L Q 2020 *Phys. Rev. Lett.* **124** 107601
[49] Zhang M R and Su Y 2022 *Int. J. Solids Struct.* **254–255** 111939
[50] Akamatsu H, Yuan Y, Stoica V A, Stone G, Yang T, Hong Z, Lei S, Zhu Y, Haislmaier R C, Freeland J W, Chen L Q, Wen H and Gopalan V 2018 *Phys. Rev. Lett.* **120** 096101
[51] Su Y, Liu N and Weng G J 2015 *Acta Mater.* **87** 293
[52] Su Y, Kang H, Wang Y, Li J and Weng G J 2017 *Phys. Rev. B* **95** 054121
[53] Picinin A, Lente M H, Eiras J A and Rino J P 2004 *Phys. Rev. B* **69** 064117
[54] Chen W J, Zheng Y, Xiong W M, Feng X, Wang B and Wang Y 2014 *Sci. Rep.* **4** 5339
[55] Li J and Weng G 2007 *Int. J. Plast.* **23** 2115
[56] Fedeli P, Cuneo F, Magagnin L, Nobili L, Kamlah M and Frangi A 2020 *Smart Mater. Struct.* **29** 095007
[57] Takeuchi T, Bétourné E, Tabuchi M, Kageyama H, Kobayashi Y, Coats A, Morrison F, Sinclair D C and West A R 1999 *J. Mater. Sci.* **34** 917
[58] Emelyanov A Y, Pertsev N A, Hoffmann-Eifert S, Böttger U and Waser R 2002 *J. Electroceram.* **9** 5
[59] Carreaud J, Bogicevic C, Dkhil B and Kiat J M 2008 *Appl. Phys. Lett.* **92** 242902
[60] Wang Z, Bin C, Zheng S and Wang J 2024 *Appl. Phys. Lett.* **125** 152903
[61] Schiøtz J, Di Tolla F D and Jacobsen K W 1998 *Nature* **391** 561
[62] Fridkin V M 2006 *Phys. Usp.* **49** 193
[63] Choudhury S, Li Y L, Chen L Q and Jia Q X 2008 *Appl. Phys. Lett.* **92** 142907

CPB Online First